

The isoperimetric problem in the hyperbolic 3-torus

Guillermo Antonio Lobos ¹, Alvaro Yucra Hanco ² and
Valério Ramos Batista ³

¹DM-UFSCar, rod. Washington Luís Km 235, São Carlos, 13565-905, Brazil

²UFT, av. Paraguai esq.c/ r. Uxiramas, Araguaína, 77824-838, Brazil

³CMCC-UFABC, av. dos Estados 5001, St André-SP, 09210-580, Brazil

*Dedicated to Professor Renato Tribuzy
on the occasion of his 75th birthday*

Abstract. The isoperimetric problem is one of the oldest in geometry, and it consists of finding a surface of minimum area that encloses a given volume V . It is particularly important in physics because of its strong relation with stability, and this also involves the study of phenomena in non-Euclidean spaces. Of course, such spaces cannot be customized for lab experiments but we can resort to computational simulations, and for this purpose one of the most widely used softwares is the Surface Evolver. In this paper we use it to study the isoperimetric problem in a hyperbolic 3-torus \mathcal{T} . More precisely: up to isometries, there exists a unique tessellation of \mathbb{H}^3 by non-ideal cubes \mathcal{C} . By identifying the opposite faces of \mathcal{C} we get \mathcal{T} . Now let Ω be a connected isoperimetric region inside \mathcal{T} . Under weak assumptions on graph and symmetry we find all numerical solutions $\Sigma = \partial\Omega$ of the isoperimetric problem in \mathcal{T} .

Keywords: Isoperimetric Problem, Hyperbolic Lattice, Surface Evolver.

2020 Mathematics Subject Classification: 49Q10.

The first author was partially supported by FAPESP proc. No. 16/23746-6, e-mail: lobos@dm.ufscar.br

1 Introduction

The isoperimetric problem is one of the oldest in geometry, and it consists of finding a surface of minimum area that encloses a given volume V . For readers not familiar with this problem we briefly comment on a physical experiment to identify possible shapes of a soap bubble inside a box. See Fig. 1.1.

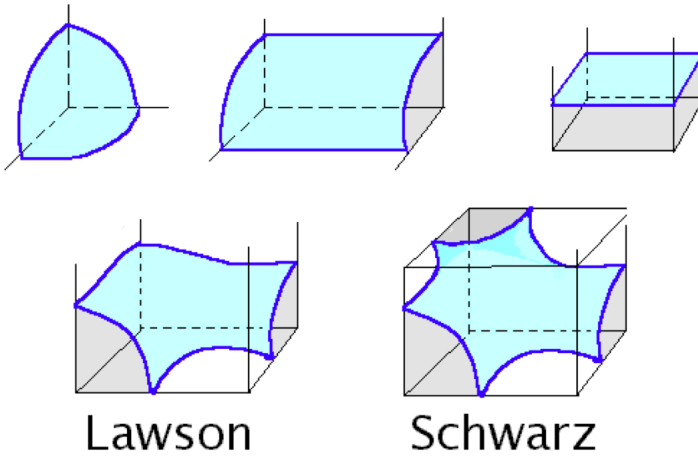


Figure 1.1: Soap bubbles in a box [29, Fig.9].

In Fig. 1.1 one must consider that tilting the box will not change the shape of the bubble, and gravity is negligible because the soap film weighs close to zero. On the top of Fig. 1.1 we can easily see the three shapes that always appear in a lab experiment: spherical, cylindrical and planar. At the bottom, on the left-hand side we have a surface found by H. Blaine Lawson, and on the right-hand side another one named after the German mathematician Karl Hermann Amandus Schwarz.

The isoperimetric problem is particularly important in physics because of its strong relation with stability, and this also involves the study of phenomena in non-Euclidean spaces. For example, by considering homogeneous density we can work with either volume V or mass m . In [22] the mathematical physicist Roger Penrose combined several results and

evidences regarding gravitational collapse in order to conjecture that, if m is the total mass and A the area of a black hole, then $4m\sqrt{\pi} \geq A$. In the theory of General Relativity this and other inequalities are called *isoperimetric inequalities for black holes* [14]. For this problem the non-Euclidean spaces of interest are the Schwarzschild and the Reissner-Nordstrom, and here we cite [10] for readers who want more details.

Differently from the example in Fig. 1.1, of course one cannot customize lab experiments with a non-Euclidean metric. But we can resort to computational simulations, and one of the softwares most widely used for this purpose is the *Surface Evolver*. Firstly introduced in 1989, now its most recent version is 2.70 [6] with numerous applications in many areas of knowledge such as Aerodynamics [3], Fluid Dynamics [9], [11], [28], and Medicine [13]. It handles forces (contact, gravity, etc.), pressures, densities, n -dimensional spaces (including non-Euclidean), tracking of quantities and prescribed energies, among several other features.

The experiment of Fig. 1.1 studies the isoperimetric problem on the flat cubic torus \mathcal{T}_0 via a cube which is a symmetric eighth \mathcal{B}_0 of its fundamental region cube \mathcal{C}_0 . The torus \mathcal{T}_0 is obtained by identifying opposite faces of \mathcal{C}_0 , and symmetry arguments show that it is enough to consider an eighth of \mathcal{C}_0 to study the isoperimetric problem. In this paper we replace \mathcal{C}_0 with a cube \mathcal{C} from an essentially unique tessellation of the hyperbolic space \mathbb{H}^3 . Identifying opposite faces yields a non-smooth \mathcal{T} , hyperbolic except for the edge singularities. We use Evolver to mimic the experiment of Fig. 1.1 on an eighth \mathcal{B} of \mathcal{C} .

In this paper we represent the hyperbolic 3-space \mathbb{H}^3 by the unit ball in \mathbb{R}^3 centred at the origin and endowed with the Poincaré metric. It is known that, up to isometries, there exists a unique tessellation of \mathbb{H}^3 by non-ideal cubes \mathcal{C} . This result is proved in Sect. 2, which also includes two weak assumptions on isoperimetric regions inside \mathcal{C} . The assumptions are needed because \mathcal{T} is too poor in space symmetries compared with a Euclidean torus \mathbb{R}^3/G , where G is a group of translations in \mathbb{R}^3 .

Notice that Fig. 1.1 does *not* show bubbles in \mathbb{R}^3/G , for this quotient

space has empty boundary. In that figure all bubbles are contained in an octant of \mathbb{R}^3/G . However, thanks to the *Aleksandrov Reflection Principle* [1] the two problems are equivalent. The same principle still holds for hyperbolic spaces (see [26]), so that we can also reduce our analysis to an octant of \mathcal{C} . Of course, in both cases we use the *Steiner-Schwarz Symmetrization*.

However, for the Euclidean case we already have strong theoretical results, and Fig. 1.1 depicts *all* possible candidates including some of the ones found in [27]. As a matter of fact, each candidate is a one-parameter family of surfaces, and the parameter is the comprised volume. More precisely, [27, Prop.6.2] characterizes the *stable* surfaces of constant mean curvature in \mathbb{R}^3/G with *positive* genus, since the sphere (also cylinder and plane) had already been known before. The author's new examples are illustrated in [27, Fig.6], which includes the unduloid (the cylinder is a special case thereof). The Lawson and Schwarz surfaces are also special cases that belong to his characterization. But in our present work we use this names from the topological point-of-view, because it is not possible to derive mathematical formulas from the numerical solutions obtained with *Evolver*.

To the best of our knowledge, \mathcal{T} still lacks a corresponding result because there the space symmetries are just quite a few. But under two weak assumptions we were able to find eight numerical candidates in Sect. 2, further reduced to only three in Sects. 3 and 4. We indicate each of these three one-parameter families in Fig. 1.2 by an *extreme* representative, namely one that is close to surpassing the interior of the octant. They were chosen because our families of solutions were analysed at their whole extension. As it happens in \mathbb{R}^3/G , one family is replaced by the other when we vary the comprised volume from zero to half of the octant's volume.

From [4] we know that any isoperimetric solution must have constant mean curvature. By looking at Fig. 1.2 left we see a numerical surface that *must* be the octant of a sphere, and this because of Erhard Schmidt's result [31] for \mathbb{H}^3 . Some readers may wonder why this octant is not centred

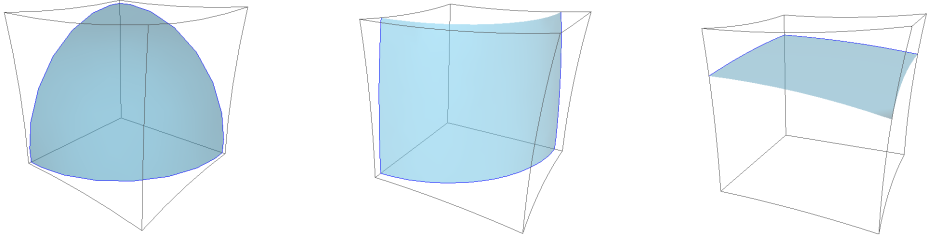


Figure 1.2: Extreme representatives of the three families of candidates.

at another vertex of \mathcal{B} . For instance, at the vertex diametrically opposite to the origin that octant would turn into a twentieth of a hyperbolic sphere by Proposition 2.1. However, the Hyperbolic Metric 2.2 seems to make equal volumes occupy more space as we move away from the origin inside \mathcal{B} . Though we cannot formalise this fact, it is possible to introduce a reasonable hypothesis, namely Assumption 2.3. It is based upon Example 2.4, and the reader will find all these settings in Sect. 2.

The same arguments apply to all examples in Fig. 1.2. In the middle we have a surface of revolution around the vertical axis through the origin. If the rotational axis were the diametrically opposite in \mathcal{B} , then we would have a fifth of a section instead of a fourth (see Fig. 2.2(b)). Once again, Assumption 2.3 discards it.

Now Fig. 1.2 centre depicts a piece of surface of revolution because of the *Steiner-Schwarz Symmetrization*, together with the *Aleksandrov Reflection Principle*. By successive reflections in the contact faces, we extend this piece to a complete surface in \mathbb{H}^3 . These surfaces were characterized in [19] (even for dimensions greater than three). A further stronger result is also given by [5] to conclude that it must be an unduloid. Of course, we have also used Theorem 2.5 in Sect. 2, which states that the surfaces in Fig. 1.2 meet the boundary of the cube *orthogonally*. This is finally applied to the example in Fig. 1.2 right, hence by successive reflections we extend it to a graph over the whole $\mathbb{H}^2 \times \{0\} \subset \mathbb{H}^3$. By [12, Thm B(c)] the extended surface must coincide with a hypersphere which, however, *cannot* be a companion of a plane in \mathbb{H}^3 . Indeed, in the upper 3d-hyperbolic

half-space model a plane can only exist perpendicular to the vertical axis, whence it is a horosphere, and therefore intersects $\partial_\infty \mathbb{H}^3$ at a single point.

For this reason we consider the eight copies of Fig. 1.2 right that result in the hyperbolic cube, which leads to the quotient 3d-space \mathcal{T} . Due to identification of sides the four upper pieces of surface will give a torus, and the same for the bottom part. That is why we call it a *pair of tori*.

In [29] Antonio Ros raises an important question: Could the Lawson surface be a solution of the isoperimetric problem for the cubic lattice in \mathbb{R}^3 ? More precisely, let us take the torus obtained by identifying the opposite faces of the unitary cube in \mathbb{R}^3 . According to [29, p.11], with *Evolver* one can get a Lawson surface of area 1.017 that encloses the volume $1/\pi$. Technically speaking, if the corresponding theoretical surface has in fact area slightly less than 1, then the answer will be *yes*. The special value $1/\pi$ will become clear in the next paragraph.

It is easy to get the area A as a function of the volume V for the three top shapes in Fig. 1.1: $A_1 = \sqrt[3]{9\pi/2} V^{2/3}$ (sphere), $A_2 = \sqrt{\pi/2} V^{1/2}$ (cylinder) and $A_3 \equiv 1/4$ (plane). Notice that $A_2 = A_3$ precisely when $8V = 1/\pi$. Fig. 1.3(a) depicts them for $0 \leq V \leq 1/16$ in blue, red and green, respectively. Fig 1.3(b) shows what happens in the corresponding hyperbolic case, which will be later detailed in Fig. 3.3(b).

For the Lawson surface A and V are both given by elliptic integrals, hence the corresponding function $A_4(V)$ has *no* explicit formula. That is why A. Ros resorted to *Evolver* for numerical values of $A_4(V)$. Its graph is always above $\min\{A_1, A_2, A_3\}$ but just by the aforementioned 1.7%, exactly when $A_2 = A_3$ at $V = 0.125/\pi$. In the hyperbolic case none of the examples in Fig. 1.2 admit an explicit $A(V)$, and Fig. 1.3(c) depicts the numerical graph of the corresponding $\min\{A_1, A_2, A_3\}$ in black compared with Lawson's example in magenta. This figure will be later detailed in Fig. 4.1(c), but here the magenta curve is at least 10% above the black one, whereas in the Euclidean case it is only 1.7% above. This is consistent with the fact that close objects in the Euclidean viewpoint turn out to be farther apart in the hyperbolic geometry.

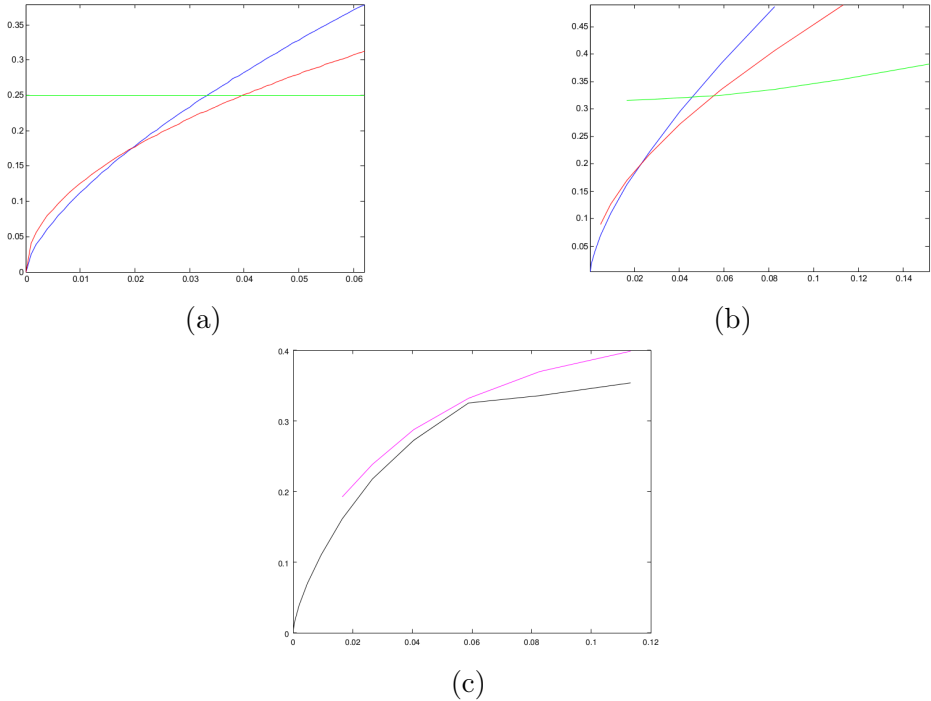


Figure 1.3: (a) Functions $A(V)$ for the Euclidean box; (b) corresponding $A(V)$ in the hyperbolic case; (c) $V \times A$ of isoperimetric solutions (black) and the Lawson surface (magenta).

The numerical gap of 10% makes it easier to prove that no Lawson surface can be isoperimetric in a hyperbolic space form: the first step is to simplify the elliptic equations that define these surfaces by means of a theoretical and accurate evaluation. See some examples in [24], [25]. By the way, [25] shows results whose numerical error is at most 0.05%. Optimistically speaking, the 1.7% could even be handled by that technique.

A. Ros’s question remains open until the present day but the corresponding question in the hyperbolic cube has a great chance to be answered because of the aforementioned results that will be obtained in Sect. 4.

Fig. 1.1 indicates that soap bubbles intersect the faces of the cube along curves of very simple topology. Our numerical solution uses the strategy

of considering all such possible topologies, which gives five cases in the hyperbolic case. Details are presented in the next section, but here we can anticipate that they were named **a**, **b**, **c**, **d** and **e**, that three letters are enough to describe the six intersections, and instead of $5^3 = 125$ cases we only have eight, as summarized in Table 2.1. Then in Sects. 3 and 4 we reduce these cases and finally obtain Table 1.1, in which *unduloid* and *pair of tori* replace the cylinder and the plane, respectively.

Table 1.1: The numerical solutions of the isoperimetric problem in an \mathbb{H}^3 lattice.

Combination	Surface
aaa	sphere
abb	unduloid
bbe	pair of tori

2 Preliminaries

This section is devoted to main theorems and propositions used throughout the text.

Proposition 2.1. *Up to isometries there exists a unique tessellation of \mathbb{H}^3 by non-ideal cubes \mathcal{C} . These cubes have dihedral angle $2\pi/5$, meaning that $n = 5$ cubes meet at each edge.*

Proof. For the uniqueness pick a vertex p of the tessellation incident to w edges. Now consider the unit sphere S^2 of the tangent space $T_p\mathbb{H}^3$. This space is isometric to \mathbb{H}^3 , whose origin is now p . Of the w edges each pair that belongs to a face of the cubic tessellation will make this face intersect with S^2 . These intersections determine a triangulation of S^2 that is both equilateral and equiangular, hence one of only three possible types: tetrahedral ($n = 3$), octahedral ($n = 4$), and icosahedral ($n = 5$). However, any hyperbolic cube has an acute dihedral angle. Therefore, only the case $n = 5$ is possible.

Now define a cube of radius R by placing vertices on the 12 geodesic rays with icosahedral symmetry emanating from p . The dihedral angle can be computed in terms of hyperbolic trigonometry: it is a continuous and strictly decreasing function of R . This function converges to $2\pi/4 = \pi/2$ for $R \rightarrow 0$, and to $2\pi/6 = \pi/3$ for $R \rightarrow \infty$. The *Intermediate Value Theorem* gives a cube \mathcal{C} with dihedral angle $2\pi/5$.

□

Lemma 2.2. *Let D be the unit disk in \mathbb{R}^2 centred at the origin. Inversion with respect to a circumference of radius r centred in $(c, 0)$ keeps D if and only if $c^2 = 1 + r^2$.*

Proof. Fig. 2.1 illustrates D in light grey and the circumference $c + r e^{i\theta}$, $0 \leq \theta < 2\pi$. By taking \mathbb{R}^2 as the complex plane we know that such inversion is

$$z \mapsto \frac{r^2}{\bar{z} - c} + c. \tag{2.1}$$

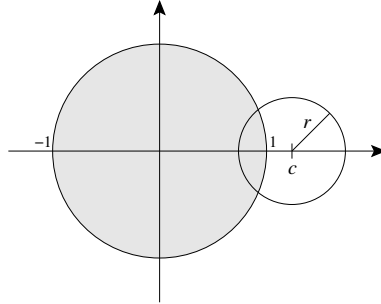


Figure 2.1: The circle D and the circumference of inversion.

In order to keep D it must interchange 1 and -1 , hence $c^2 = 1 + r^2$. Notice that (2.1) takes the origin to $1/c \in D$. Conversely, if $c^2 = 1 + r^2$ then (2.1) becomes $(c\bar{z} - 1)/(\bar{z} - c)$, which obviously keeps ∂D . But since we have $0 \mapsto 1/c < 1$ then it keeps D .

□

Proposition 2.1 allows us to define a lattice of isometries in \mathbb{H}^3 which keeps the cubic tessellation. Consider the three pairs of opposite faces of

\mathcal{C} . For each such pair there is a mirror reflection $\sigma_1, \sigma_2, \sigma_3$ in one of the faces, and there are also mirror reflections τ_1, τ_2, τ_3 which flip only the pair of opposite faces (and fix the midpoint of \mathcal{C}). The latter are represented by mirror reflections in the three coordinate planes in Fig. 2.2(a). From Lemma 2.2 the formers are represented by spherical inversions such as

$$q \mapsto r^2 \cdot \frac{q - (c, 0, 0)}{\|q - (c, 0, 0)\|^2} + (c, 0, 0),$$

where $c = (\sqrt{5} + 2)^{1/2}$ and $r = (\sqrt{5} + 1)^{1/2}$. These are the values that keep the tiling $\{4, 5\}$ depicted in Fig. 2.2(b). Now we compose $T_i := \tau_i \circ \sigma_i$ to obtain a “translation”, namely an isometry of hyperbolic type. Finally we let $\Gamma := \langle T_1, T_2, T_3 \rangle$ and take the orbit $Orb(\mathcal{C})$, whence $\mathcal{T} := Orb(\mathcal{C})/\Gamma$.

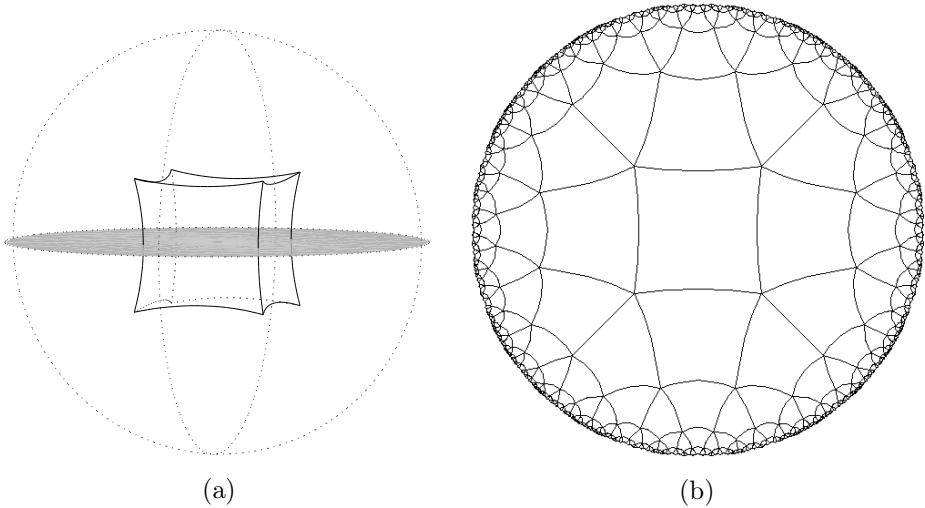


Figure 2.2: (a) The cube \mathcal{C} ; (b) the tiling $\{4, 5\}$.¹

By means of the *Aleksandrov Reflection Principle* [1] we can reduce our study of the isoperimetric problem to a symmetric eighth $\mathcal{B} \subset \mathcal{C}$. In the Poincaré model if \mathcal{C} is as in Fig. 2.2(a) then $\mathcal{B} := \mathcal{C} \cap \{x_1 \geq 0\} \cap \{x_2 \geq 0\} \cap \{x_3 \geq 0\}$. If V denotes hyperbolic volume then $V(\mathcal{C}) \cong 1.723$ and

¹From <https://mathcs.clarku.edu/~djoyce/poincare/tilings.html>

$V(\mathcal{B}) \cong 0.215$. These values were obtained through the *Surface Evolver*, whose details are given in Sect. 3.

The conformal metric in \mathbb{H}^3 is given by

$$\frac{4 I_3}{(1 - x_1^2 - x_2^2 - x_3^2)^2}, \tag{2.2}$$

where I_3 is the 3×3 identity matrix. For instance, if we consider a Euclidean radius $\varepsilon \in (0, 1)$ and the corresponding sphere S_ε centred at the origin, the area of and volume inside $S_\varepsilon \subset \mathbb{H}^3$ are given by

$$A(S_\varepsilon) = \frac{16\pi\varepsilon^2}{(1 - \varepsilon^2)^2} \quad \text{and} \quad V(S_\varepsilon) = 2\pi \left[\frac{2\varepsilon(1 + \varepsilon^2)}{(1 - \varepsilon^2)^2} + \ln \frac{1 - \varepsilon}{1 + \varepsilon} \right], \tag{2.3}$$

respectively. Notice that both $A(S_\varepsilon)$ and $V(S_\varepsilon)$ are strictly increasing with ε . As mentioned at the Introduction, in this work we adopt two assumptions on isoperimetric regions in \mathcal{B} .

Assumption 2.3. Any isoperimetric region in \mathcal{B} intersects the three coordinate planes.

As a matter of fact we believe that Assumption 2.3 is always true but were not able to prove this fact yet. Up to ambient isometries it is valid in Euclidean three-dimensional boxes, as proved in [27]. For now here is an example that motivates Assumption 2.3:

Example 2.4. The set $T_1 := S_\varepsilon \cap \mathcal{B}$ encloses volume $V(S_\varepsilon)/8$. Now let S be a sphere centred at the upper right corner of the central square in Fig. 2.2(b), which in Euclidean coordinates corresponds to $(\mathbf{c}, \mathbf{c}, 0)$ where

$$\mathbf{c} = \frac{\sqrt{\sqrt{5} + 2} - \sqrt[4]{5}}{2}. \tag{2.4}$$

If $T_2 := S \cap \mathcal{B}$ encloses the *same* volume $V(S_\varepsilon)/8$ then $V(S) = 5V(S_\varepsilon)/4$ and therefore $A(T_2) > A(T_1)$.

Now we present a strong result that will be widely used in our work. According to [29], from [2], [16], [18], [21] we have:

Theorem 2.5. *Suppose $M^3 \subset \mathcal{C}$ is compact and ∂M is either empty or piecewise smooth. Then for any $t \in (0, V(M))$ there exists a compact domain $\Omega \subset M$ such that $\Sigma = \partial\Omega \setminus \partial M$ minimizes area among regions of volume t . Moreover, the boundary of any minimizing region is a smooth embedded surface with constant mean curvature and, if $\partial M \cap \Sigma \neq \emptyset$, then Σ meets ∂M orthogonally.*

Any Σ that minimizes area under volume constraint has *constant mean curvature* (CMC). For instance, see [4] to check this well-known property. In their turn CMC surfaces follow the *maximum principle* (see [15]), which is the key to conclude that $\partial M \perp \Sigma$ whenever $\partial M \cap \Sigma \neq \emptyset$. The property of orthogonal intersections will be used extensively in this work. The following result is an important clue on Assumption 2.3:

Proposition 2.6. *Let Ω be an isoperimetric region of \mathcal{B} and $\Sigma = \partial\Omega \setminus \partial\mathcal{B}$. Then $\partial\Omega \setminus \Sigma$ cannot contain open subsets of only zero, one, or two incident faces of $\partial\mathcal{B}$. In particular we have $\partial\mathcal{B} \cap \Sigma \neq \emptyset$.*

Proof. Let us apply Theorem 2.5 to $M = \mathcal{B}$. By contradiction, consider a continuous family $\{\phi_t : t \in [0, 1]\}$ of hyperbolic isometries that leave invariant the zero, one, or two coordinate planes. Let ϕ_0 be the identity and $\phi_1(\mathcal{B}) \cap \mathcal{B} = \emptyset$. Now if Ω intersects only zero, one, or two incident faces, then we consider for the respective family ϕ_t the supremum T of the values t such that $\phi_t(\Omega) \subset \mathcal{B}$. Since ϕ_T keeps $V(\Omega)$ then $\phi_T(\Omega)$ is also minimizing. However, $\phi_T(\Omega)$ touches $\partial\mathcal{B}$ tangentially, and so violates $\partial M \perp \Sigma$.

□

Because of Proposition 2.6 successive reflections of Σ in the coordinate planes will result in a potential solution of the isoperimetric problem for $t = 8V(\Omega)$ in the torus \mathcal{T} (equivalently in its fundamental domain \mathcal{C}).

Next we are going to adopt the term *two-dimensional graph* as the graph of a function of one variable. Of course, the graph will be connected if the function is continuous.

Assumption 2.7. Let Σ be as in Proposition 2.6. Then its intersection with any coordinate plane is either empty or a two-dimensional connected graph.

In this paper we analyse Σ under Assumptions 2.3 and 2.7. A little reflection shows that for $1 \leq i < j \leq 3$ there are only four non-empty possible connected topological cases depicted in Fig. 2.3. Notice that Fig. 2.3(b) is a graph in both directions since our geometry is hyperbolic. Moreover, we shall see that the numerical candidates for this case are either unduloids or a pair of equidistant tori.

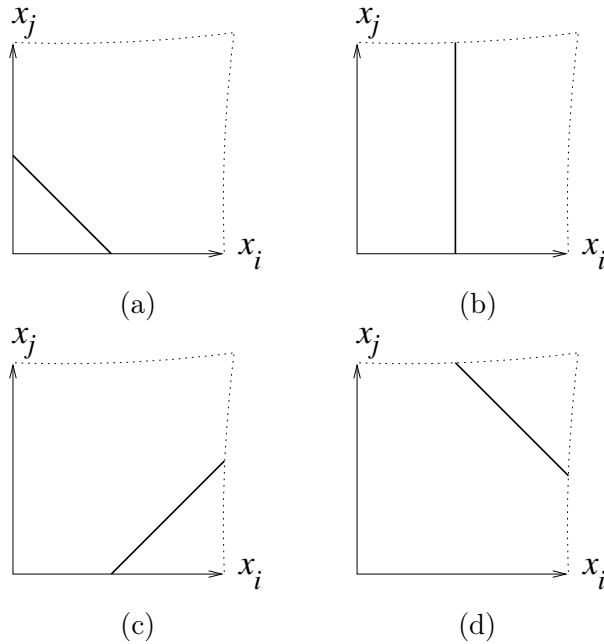


Figure 2.3: The four possible non-empty graph types in $Ox_i x_j$.

Not all combinations of the three axes are feasible. Table 2.1 shows the eight possible combinations and the name we attribute for each one. The empty graph is called “e”, the triad of letters $\ell_1 \ell_2 \ell_3$ corresponds to $Ox_1 x_2$, $Ox_1 x_3$ and $Ox_2 x_3$ in this order, respectively. More details on Table 2.1 will be given in Sect. 4. There we explain why **acc** is called *inverted Lawson*,

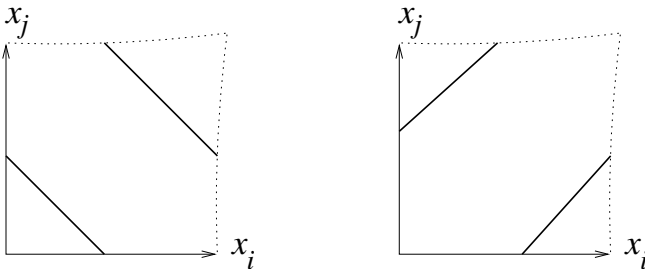
Table 2.1: Triad of letters and some known examples.

Combination	Surface
aaa	sphere
abb	unduloid
abc	
acc	inverted Lawson
bbd	Lawson
bbe	pair of tori
bcd	
ddd	Schwarz

and why some cases like bce , ccd and dde are not included. Notice that $\ell_1\ell_2\ell_3$ is always in alphabetical order because of congruence. For example, acb is congruent to abc .

The isoperimetric problem considers $V(\Omega) \leq V(\mathcal{B})/2 \cong 0.108$. We could also take the origin $O \in \Omega$ but for the sake of visibility some cases in Table 2.1 are studied for $O \notin \Omega$.

Before going ahead one should notice that Assumption 2.7 requires the graph to be connected. Otherwise one should consider another two extra cases depicted in Fig. 2.4. But later we shall see that they perform worse than the candidates listed in Table 2.1, which thus omitted them.

Figure 2.4: The two possible non-connected graph types in Ox_ix_j .

3 Evolver datafiles

In order to study each case numerically we make use of the *Surface Evolver* [7], [8]. For lengths and areas *Evolver* computes Riemannian values through the metric given in the datafile. However, volumes must be achieved as a declared quantity and the computation does not use the given metric any longer. Therefore, we implemented the submanifold quantity `sbmvol` in order to have

$$\int_M 1dV = \int_M \frac{8 dv}{(1 - x_1^2 - x_2^2 - x_3^2)^3}, \tag{3.1}$$

where dV and dv are the hyperbolic and Euclidean elements of volume, respectively.

But *Evolver* only computes *surface integrals* (line integrals are in fact sums of thin strips of surface). So we need to introduce a vector field $(\mathbf{q}_1, \mathbf{q}_2, \mathbf{q}_3)$ in such a way that its divergence is $8/(1 - x_1^2 - x_2^2 - x_3^2)^3$. By setting $\rho = x_3/\sqrt{1 - x_1^2 - x_2^2}$ we may first compute

$$\int \frac{8d\rho}{(1 - \rho^2)^3} = \frac{2\rho}{(1 - \rho^2)^2} + \frac{3\rho}{1 - \rho^2} + \frac{3}{2} \ln \frac{1 + \rho}{1 - \rho}. \tag{3.2}$$

Hence, if we take $\mathbf{q}_1, \mathbf{q}_2$ as identically zero then \mathbf{q}_3 is given by

$$\int \frac{8dx_3}{(1 - x_1^2 - x_2^2 - x_3^2)^3} = \frac{2x_3}{(1 - x_1^2 - x_2^2 - x_3^2)^2(1 - x_1^2 - x_2^2)} + \frac{3x_3}{(1 - x_1^2 - x_2^2 - x_3^2)(1 - x_1^2 - x_2^2)^2} + \frac{3/2}{(1 - x_1^2 - x_2^2)^{5/2}} \ln \left| \frac{\sqrt{1 - x_1^2 - x_2^2} + x_3}{\sqrt{1 - x_1^2 - x_2^2} - x_3} \right|. \tag{3.3}$$

In this way $(\mathbf{q}_1, \mathbf{q}_2, \mathbf{q}_3)$ are not symmetric. A better choice is to compute \mathbf{q}_1 and \mathbf{q}_2 as done for \mathbf{q}_3 , and then take one third of each expression. That is what we use in the datafiles.

Moreover, notice that Assumption 2.3 and Theorem 2.5 enable us to study the isoperimetric regions $\Omega \subset \mathcal{B}$ in such a way that the computation of the volume $V(\Omega)$ will not use $\partial\Omega \cap \partial\mathcal{B}$. For instance, the face of Σ on $x_3 = 0$ makes (3.3) vanish, and the analogous holds for the symmetric

(q1,q2,q3) used in our datafiles. Hence we can work with $\Sigma = \partial\Omega \setminus \partial\mathcal{B}$, as described in Proposition 2.6.

Inside \mathcal{C} the sphere S_ε centred at the origin cannot have $\varepsilon \geq \varepsilon = c - r \cong 0.26$. Namely, for the first line of Table 2.1 our simulation takes $\varepsilon \in (0, \varepsilon)$. With *Evolver* 2.70 and *Geomview* 1.9.4 we obtained Fig. 3.1(a). It depicts the numerical surface, whereas Fig. 3.1(b) shows $V \times A$ for (2.3) and Fig. 3.1(c) the corresponding $V \times \Delta A$, where ΔA is the difference between numerical and theoretical values of area.

In our simulation *Evolver* reached numerical values of volume that coincide with the theoretical ones up to the 8th decimal. Hence we consider them as identical. In Fig. 3.1(c) we have $\Delta A \leq 0.00163$, and the abrupt change at $V \cong 0.02$ just means that we refined the triangulation for that volume. This is to guarantee that $A/F \leq 0.01$, where F is the number of triangles. The fact that $V \leq V_\varepsilon \cong 0.083$ can be seen in Fig. 3.1(b), namely less than $V(\mathcal{B})/2 \cong 0.108$, which means a great difference from the Euclidean case. Indeed, if that eighth of cube were Euclidean the extreme **aaa** would have more than half of its volume.

Now back to Table 2.1 we consider **abb**. Numerically speaking this case is rather different from **aaa**, in which the initial surface was just a tiny equilateral triangle with vertices on the coordinate axes. As usual, *Evolver* starts with a very simple polyhedral surface whose triangulation must be consistently refined, equalised and submitted to energy minimisation under geometrical and quantitative constraints. After some iterations the numerical surface may serve as evidence to help answer theoretical questions.

For **abb** we could try the initial surface depicted in Fig. 3.2(a). It consists of a rectangular blue face and a transparent triangular face on top. This one is used by (q1,q2,q3) to compute the hyperbolic volume but we ask *Evolver* to paint it in **CLEAR** for $A(\Sigma)$ does not count it.

We end up with a numerical unduloid by starting from Fig. 3.2(a). But it presents two numerical problems: the convergence is slow and the resulting unduloid is just a local minimum of area under volume constraint.

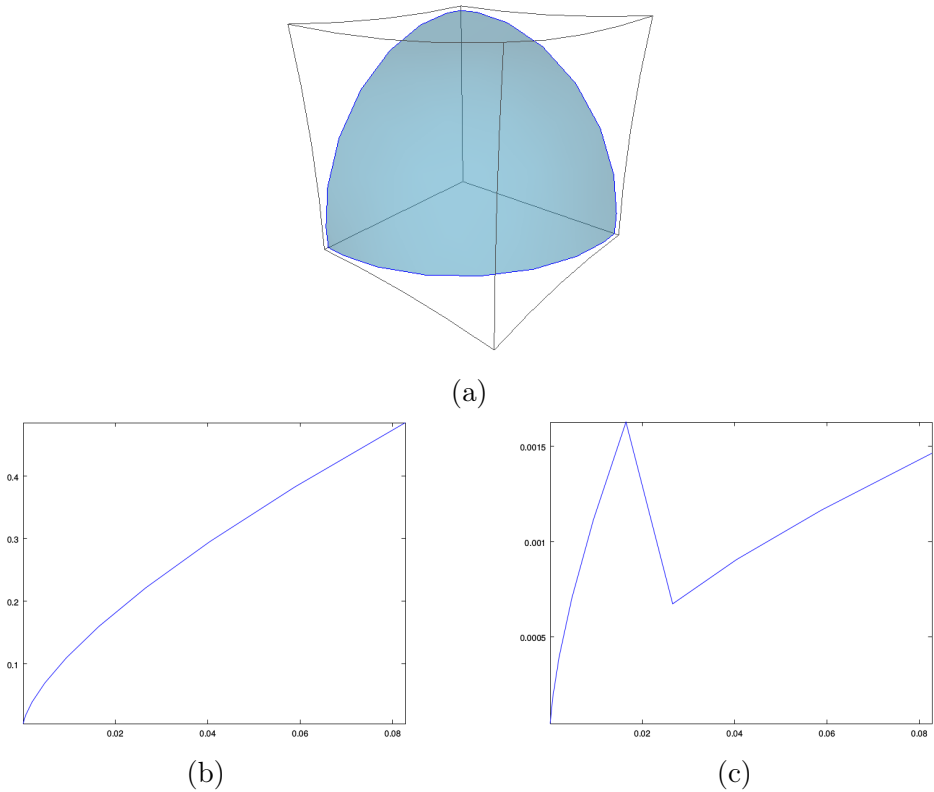


Figure 3.1: (a) Case **aaa** for $\varepsilon \cong \varepsilon$; (b) graph $V \times A$; (c) difference between values of area.

The convergence problem arises from the long thin shape and the initial contact angle of circa $\pi/4$ with the coordinate planes. It does converge to $\pi/2$ as expected from Theorem 2.5 but not as quickly as **aaa**, since now we have that long thin face.

The non-isoperimetric unduloid arises from the metric (2.2), which makes the blue face in Fig. 3.2(a) broad on top and narrow on bottom. That is the feature we get for the resulting surface, which is just a local minimum under volume constraint. From the Euclidean perspective the isoperimetric unduloid must look broader on bottom than on top, which is the case if we start from Fig. 3.2(b). Notice that the initial surface is

also orthogonal to $\partial\mathcal{B}$, which speeds up convergence to a numerical answer compatible with Theorem 2.5.

These strategies may look rather tricky but when dealing with numerical optimisation either *Evolver* or any other software will strive for convergence around values that are potentially local minima. Global minima will be hardly found without applying theoretical framework.

That said, we generated unduloids of volume $V(S_\varepsilon)$ according to (2.3) for ε varying from $2\varepsilon/5$ to $6\varepsilon/5$. This last one is depicted in Fig. 3.2(c). Finally, Fig. 3.2(d) shows both **aaa** and **abb** for $V \times A$. There the **abb** and **aaa** curves are red and blue, respectively (cf. Fig. 3.1(b)). Notice the turning point at $V \cong 0.022$.

Unduloids like in Fig. 3.2(c) are surfaces obtained by revolution of a stretch of *hypercircle* around Ox_3 . If we take Ox_1, Ox_3 as the horizontal and vertical axes in Fig. 2.2(b), respectively, then hypercircles are all equated as

$$(x_1 + (1/\varepsilon - \varepsilon)/2)^2 + x_3^2 = (1/\varepsilon + \varepsilon)^2/4, \quad (3.4)$$

in our case restricted to $\varepsilon < \varepsilon$ and $x_3 < c - (r^2 - x_1^2)^{1/2}$ in Euclidean values. This motivates the following definition:

Definition 3.1. Consider the curve (3.4) in Ox_1x_3 for positive $x_3 < c - (r^2 - x_1^2)^{1/2}$ and $\varepsilon < \varepsilon$. Then U_ε is the surface of revolution obtained by rotation of this curve around Ox_3 . We call U_ε the vertical unduloid with axis Ox_3 .

Back again to Table 2.1 we now take **bbe**, a much easier case from the numerical point-of-view. For $V = 0$ the corresponding $A = \mathcal{A}$ is one quarter of the area of the central square in Fig. 2.2(b). By means of polar coordinates we get

$$\pi + \mathcal{A} = \int_0^{\pi/4} \frac{2}{1 - c^2 \cos^2 \theta + c \cos \theta \cdot \sqrt{c^2 \cos^2 \theta - 1}} = \frac{11}{10} \pi, \quad (3.5)$$

where the value in (3.5) was computed via *Cauchy's Residue Theorem*. Namely, we begin with $A = \pi/10$ and A does not grow very much with

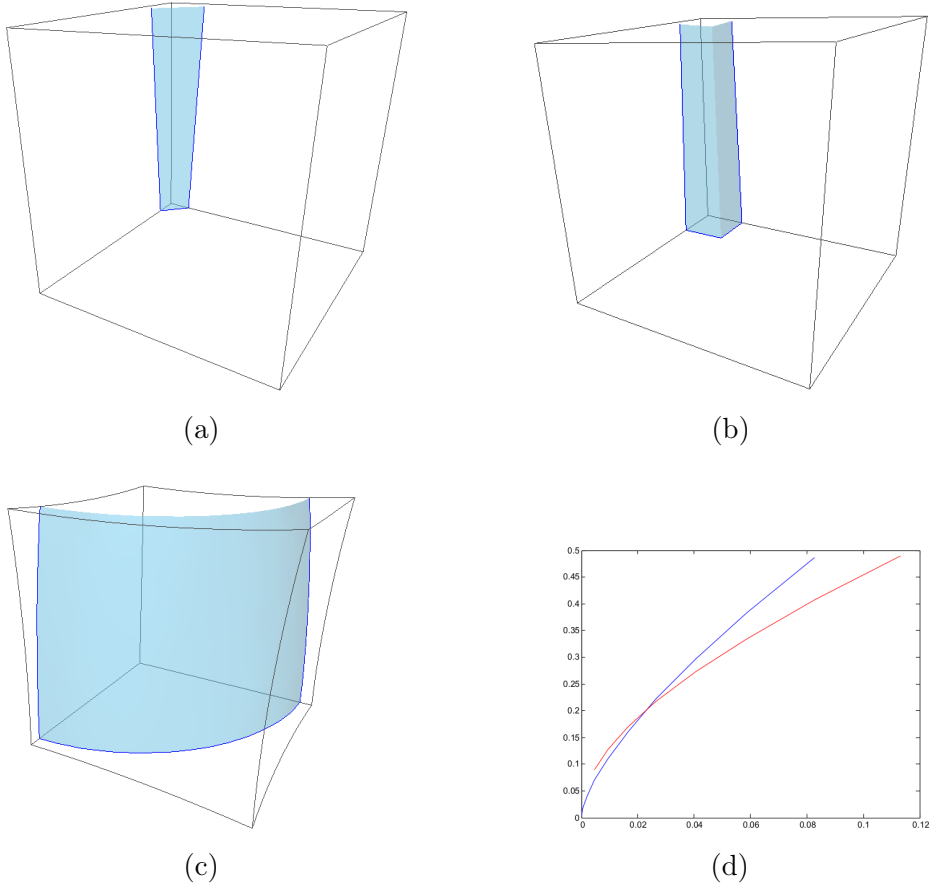


Figure 3.2: (a) Initial abb ; (b) with adjustments; (c) extreme unduloid; (d) $aaa \times abb$.

V . Of course, it is constant in the Euclidean case. In Fig. 3.3(a) we see $A \cong 0.38$ for the extreme value $V \cong 0.15$, which already surpasses $V(\mathcal{B})/2 \cong 0.108$. The turning point between abb and bbe is at $V \cong 0.058$, as shown in Fig. 3.3(b). It summarizes the three main cases for our discussions in the next section.

Of course, from (3.4) we see that the surface in Fig. 3.3(a) is a piece of *hypersphere* equated as

$$x_1^2 + x_2^2 + (x_3 + (1/\varepsilon - \varepsilon)/2)^2 = (1/\varepsilon + \varepsilon)^2/4, \tag{3.6}$$

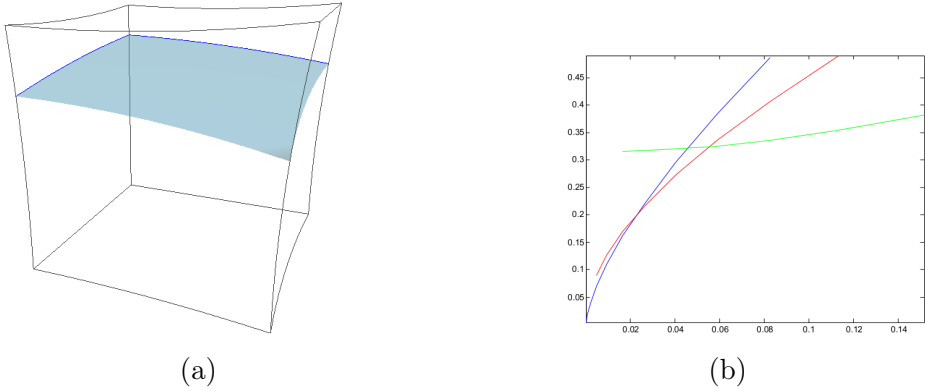


Figure 3.3: (a) Extreme **bbe**; (b) joint graph of **aaa**, **abb** and **bbe**.

where $\varepsilon < \varepsilon$ and x_1, x_2 vary inside the positive quadrant of the central square in Fig. 2.2(b).

4 Results

At the Introduction we mentioned an important result from [29, p.11]: with *Evolver* one obtains a Lawson surface of area 1.017 that encloses the volume $1/\pi$. Namely, if the area of the theoretical surface lies under 1, then Lawson's example becomes an isoperimetric solution in the unitary Euclidean cube.

Fig. 4.1(a) summarizes the corresponding three cases for a cubic lattice of \mathbb{R}^3 . Lawson's hyperbolic surface is depicted in Fig. 4.1(b) with $A \cong 0.399$ for $V \cong 0.113$, already above $V(\mathcal{B})/2 \cong 0.108$. Similarly to the other numerical examples the Lawson and Schwarz surfaces are obtained by letting *Evolver* expand a given prototype, as can be seen from Figs. 3.2(a) and (b), whence this one generated the family of unduloids with an extreme member depicted in Fig. 3.2(c). Our *Evolver* scripts include a routine to save computed area values A , each one corresponding to a given volume V , all sorted on a list. The obtained pairs (V, A) are plotted with Octave, as depicted in Fig. 3.2(d). The script files will be made available at <https://>

[//sites.google.com/site/vramos1970](https://sites.google.com/site/vramos1970) in the short future.

For reasons that will soon be explained the minimum of the three graphs in Fig. 3.3(b) will be called *the isop-curve*. This curve is compared with the graph $V \times A$ in magenta of our simulation of Lawson’s case (see Fig. 4.1(c)).

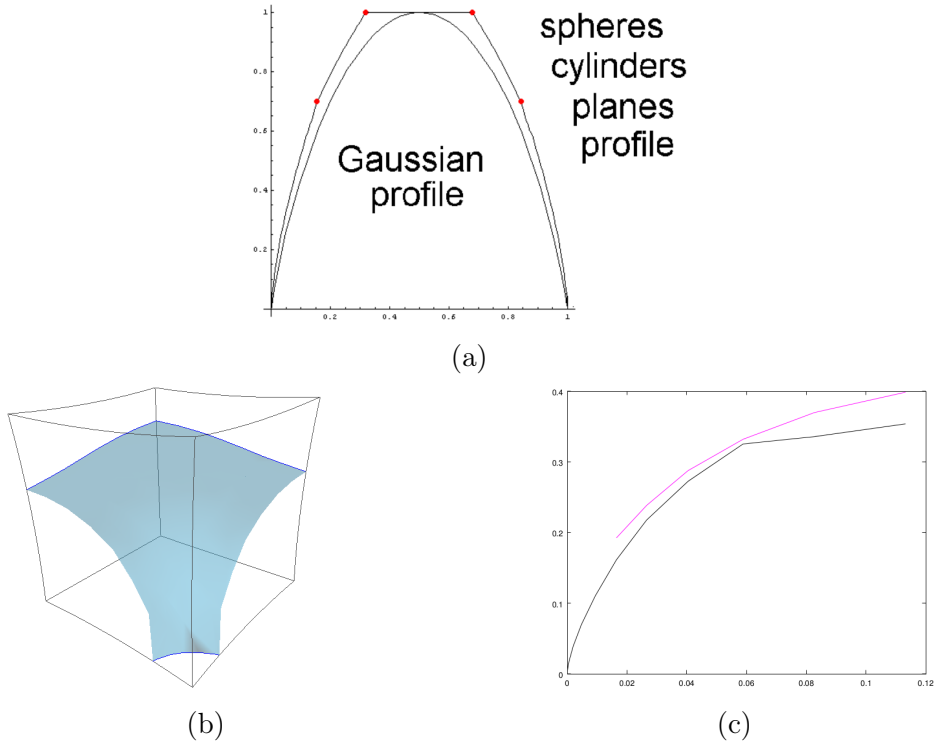


Figure 4.1: (a) The Euclidean case from [29, Fig.10]; (b) extreme Lawson; (c) $\text{bdd} \times \text{isop-curve}$ in magenta and black, respectively.

In Fig. 4.1(a) the turning points occur at circa 0.15 and 0.3, respectively. Since $V(\mathcal{B}) \cong 0.215$ our first and second turning points occur for the ratios $0.022/V(\mathcal{B}) \cong 0.102$ and $0.058/V(\mathcal{B}) \cong 0.27$, respectively. Roughly speaking, they happen *earlier* than for the Euclidean case. This explains why the bdd -curve is visibly above the isop -curve in Fig. 4.1(c).

We used (2.3) to make the bdd -curve start at $V(S_\varepsilon) \cong 0.016$ for $\varepsilon =$

$3\varepsilon/5$. In Fig. 3.2(d) the unduloid started at $V(S_\varepsilon) \cong 0.005$ for $\varepsilon = 2\varepsilon/5$. In theory an unduloid can have arbitrarily small volume but numerical simulations will only be meaningful if we avoid extreme cases. With the Lawson surface there is an additional problem: it simply does not exist when V is too little. In our simulations, for V slightly below 0.016 ($\varepsilon < 3\varepsilon/5$) the initial surface converges to a degenerate surface consisting of an eighth of S_ε connected to $(\varepsilon, 0, 0)$ and $(0, \varepsilon, 0)$ by tiny tubes.

The analogous problem occurs with **acc**. Topologically speaking, this case is obtained through a Euclidean reflection of **bbd** in the plane determined by the points $(\varepsilon, 0, 0)$, $(0, \varepsilon, 0)$, $(\mathfrak{c}, 0, \mathfrak{c})$ and $(0, \mathfrak{c}, \mathfrak{c})$, where \mathfrak{c} is defined in (2.4). This plane works as a mirror that inverts the way we see the Lawson surface, hence the name *inverted Lawson*.

In the Euclidean cube of edglength \mathfrak{c} the inverted Lawson is again the Lawson surface but translated by $(\mathfrak{c}, \mathfrak{c}, 0)$. However, in the hyperbolic cube we get a different graph $V \times A$ for the inverted surface. This is due to the metric (2.2), which requires more area $A(\Omega)$ to comprise the same volume $V(\Omega)$ when Ω leaves the origin (see Example 2.4 in Sect. 2). Fig. 4.2(a) shows an inverted Lawson close to the extreme case of collapsing its handle around O with the origin itself. Fig. 4.2(b) shows the $V \times A$ graph for **acc** in blue, together with the other graphs in Fig. 4.1(c).

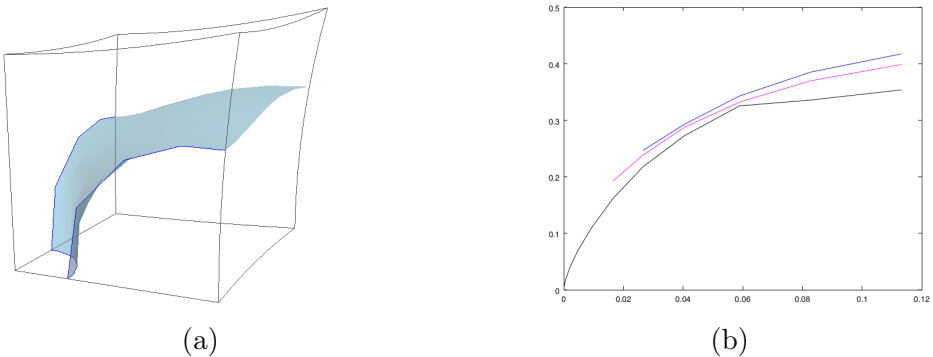


Figure 4.2: (a) Extreme inverted Lawson; (b) **acc** in blue, **bbd** and the isop-curve.

Since we have just recalled Example 2.4, notice that its arguments also

work for unduloids:

Example 4.1. Take U_ε, U instead of S_ε, S , respectively, where U_ε is given by Definition 3.1 and U is the “inverted U ”, as explained right above. Namely, $V(U) = 5V(U_\varepsilon)/4$ and therefore $A(U \cap \mathcal{B}) > A(U_\varepsilon \cap \mathcal{B})$. In the case of a horizontal unduloid, namely with axis either Ox_1 or Ox_2 , area and volume remain unchanged for the “inverted” surface.

In Example 4.1 the assertion about horizontal unduloids comes from the fact that their “inversion” can be equated. For the axis Ox_2 it is the composition of two isometries in \mathbb{H}^3 : 90° -rotation $(x_1, x_2, x_3) \mapsto (x_2, -x_1, x_3)$ followed by the spherical inversion

$$q \mapsto 2r(c+r) \cdot \frac{q - (c+r, 0, 0)}{\|q - (c+r, 0, 0)\|^2} + (c+r, 0, 0).$$

For the axis Ox_1 it is $(x_1, x_2, x_3) \mapsto (-x_2, x_1, x_3)$ followed by

$$q \mapsto 2r(c+r) \cdot \frac{q - (0, c+r, 0)}{\|q - (0, c+r, 0)\|^2} + (0, c+r, 0). \tag{4.1}$$

Because of Examples 2.4 and 4.1 we had already expected the **acc**-graph to lie above the **bbd**-graph as depicted in Fig. 4.2(b). For the sake of concision we could then have skipped the numerical analysis of **acc**. Nevertheless, it is important to include it here for two reasons: it justifies why Table 2.1 omits even some feasible cases (like **ccd** and **dde**), and it helps to check the reliability of our numerical simulations as we are going to do right now.

Indeed, **acc** above **bbd** was already expected but we can look even closer. The factor $5/4$ is due to the five-fold symmetry on the corners instead of the four-fold symmetry at the centre of any square in Fig. 2.2(b). In the Euclidean case any 3D-manifold whose dimensions increase by the same factor λ will get A, V increased by λ^2 and λ^3 , respectively. For a cylinder of constant height we have the same factor λ for both A, V if top and bottom do not count. Roughly speaking the Lawson surface is close to a pair of horizontal unduloids connected by a very small piece of sphere.

By means of Taylor expansion we rewrite (2.3) as

$$A(S_\varepsilon) = 16\pi\varepsilon^2 + \mathcal{O}(\varepsilon^4) \quad \text{and} \quad V(S_\varepsilon) = \frac{32}{3}\pi\varepsilon^3 + \mathcal{O}(\varepsilon^5). \quad (4.2)$$

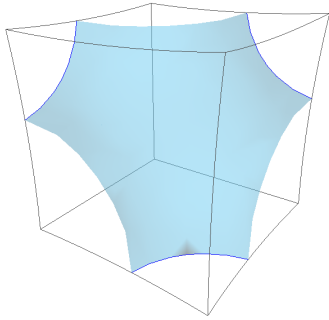
Namely A grows by $(5/4)^{2/3} \cong 1.16$ when V grows by $5/4$, but its contribution to the Lawson surface must be less than that. As we have already explained in Example 4.1, the pair (V, A) remains unchanged for horizontal unduloids. Therefore A must grow very little for the inverted Lawson, as we see in Fig. 4.2(b). The growth ratio varies from 1.03 to 1.05 according to our numerical tests.

A little reflection shows that **bce** is the “inversion” of **bdb**, this one congruent to the Lawson surface, and now we have arguments to skip **bce**. Table 2.1 also omits **ccd** because it is the “inverted” **bcd**. One obtains **dde** by taking the “inversion” of **abc** with respect to the rectangle $(\varepsilon, 0, 0)$, $(0, 0, \varepsilon)$, $(\mathbf{c}, \mathbf{c}, 0)$, $(0, \mathbf{c}, \mathbf{c})$, hence this one was omitted from Table 2.1 as well.

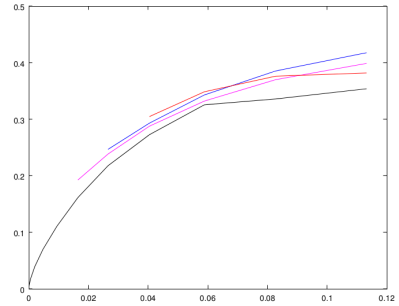
Now we are going to study **ddd**, namely the Schwarz surface in Table 2.1. For reasons that we have already explained for the case of the Lawson surface, it is already expected that the Schwarz surface does not exist for too little volume. Indeed, our numerical experiments show that the initial surface degenerates to a piece of sphere connected to $(\varepsilon, 0, 0)$, $(0, \varepsilon, 0)$ and $(0, 0, \varepsilon)$ by tiny tubes when V is very small. We begin with V_ε for $\varepsilon = 4\varepsilon/5$ until $\varepsilon = 11\varepsilon/10$ when the volume surpasses $V(\mathcal{B})/2 \cong 0.108$. See Fig. 4.3(a) for an illustration and also Fig. 4.3(b) for its graph $V \times A$ in red.

For the readers who want to have an overview of Schwarz’s surface with zero CMC in \mathbb{H}^3 here is a nice picture by Konrad Polthier (Freie Universität Berlin): http://www.polthier.info/articles/teaser/H3wrfeb_tiny.jpg

Now what is the *inverted Schwarz*? By looking at Figs. 2.3(a) and (c) we realise that it should be again **acc**, which was called *inverted Lawson*. However, by arguments already given in this section we know that “inversion” leads to a non-isoperimetric Σ and for this reason we do not care about the apparent dubious meaning of **acc**. The *inverted Schwarz* can then be skipped, even if Fig. 2.3 leaves only **acc** as a way to codify it. For



(a)

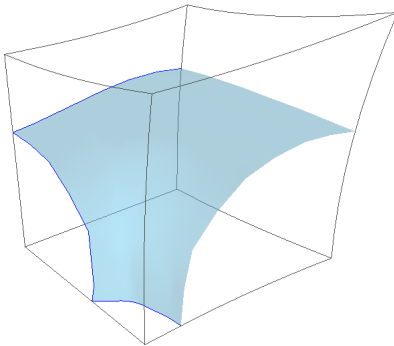


(b)

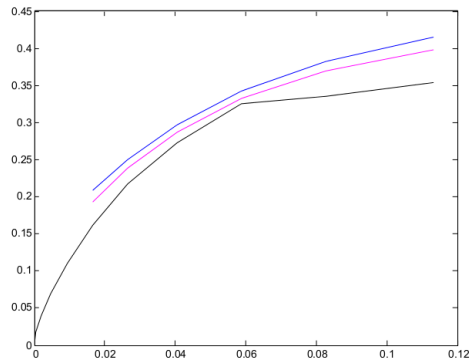
Figure 4.3: (a) Extreme Schwarz; (b) **ddd** in red and the previous curves.

the same reason we shall not differ sub-cases when dubious triads $\ell_1\ell_2\ell_3$ appear again.

Back to Table 2.1 we now study the remaining cases **abc**, **bcd** and **bce**. Topologically speaking Fig. 4.4(a) shows that these surfaces are Lawson’s example reflected by (4.1). But differently from the previous inverted cases now we must analyse these ones numerically. Fig. 4.4(b) compares **abc** with Fig 4.1(c).



(a)



(b)

Figure 4.4: (a) Extreme **abc**; (b) **abc** in blue, **bbd** and the isop-curve.

By looking at Figs. 4.4(b) and 4.2(b) we realise that **abc** is quite similar to the inverted Lawson. But **abc** lies above **bbd** almost as a parallel curve

while **acc** rises more quickly and is closer to **bbd** for small values of V . Anyway, we still can argue that **abc** needs more area for the same volume of **bbd** because the contact of **abc** with the origin is not as “large” as in the case of **bbd**. Together with the metric (2.2) this explains why **abc** performs worse than **bbd**.

Finally we are going to study **bcd**, which is in fact a degenerate case. From Figs. 4.5(a) to (c) one promptly recognises that its topology was discarded as a possible CMC surface in a Euclidean three-dimensional box, as proved in [27, Prop.6.2]. Indeed, there the only examples of genus three that are stable CMC surfaces must have the same topology of Schwarz’s surface, which is obviously not the case in Figs. 4.5(a) to (c). We refer the reader to [27, Fig.6] for an illustration.

However, since we cannot adapt all of the arguments in [27] to the hyperbolic geometry, and similar CMC surfaces were already found in Euclidean boxes (see the gyroids of [17, Fig.2]), then we must include the numerical analysis of this case. The volume $V \cong 0.058$ is fixed and the area A decreases in Figs. 4.5(a) to (c). Namely, no CMC surface can be found in \mathcal{B} with that topology.

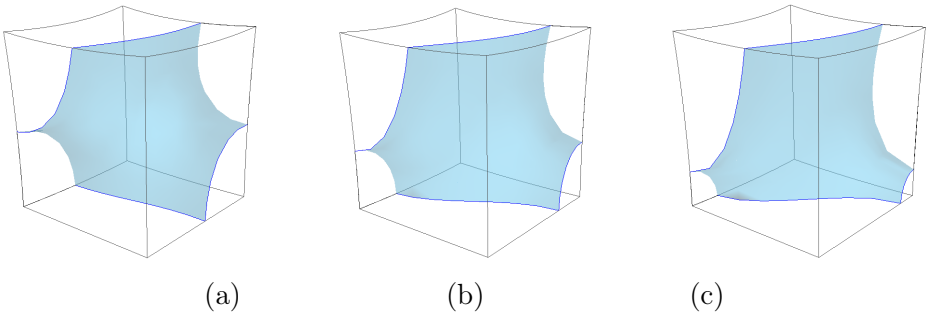


Figure 4.5: The degenerate case **bcd**: (a) initial smoothed surface; (b) evolving once; (c) close to degeneration.

We conclude this section with a brief comment on the cases depicted in Fig. 2.4. One of them is combined with **aa** and presented in Fig. 4.6. It looks like a Lawson surface rotated by 45° around Ox_3 . What is a con-

gruence in the Euclidean case changes drastically in \mathcal{B} . Fig. 4.6 shows an example with $V \cong 0.04$ and $A \cong 0.328$, namely well above the corresponding V for the magenta curve in Fig. 4.1(c). The magenta curve starts at $V \cong 0.016$ but now what happens for V slightly below 0.04 is that the surface degenerates to a pair of eighths of sphere centred at O and $(\mathbf{c}, \mathbf{c}, 0)$ and connected by a tiny tube.

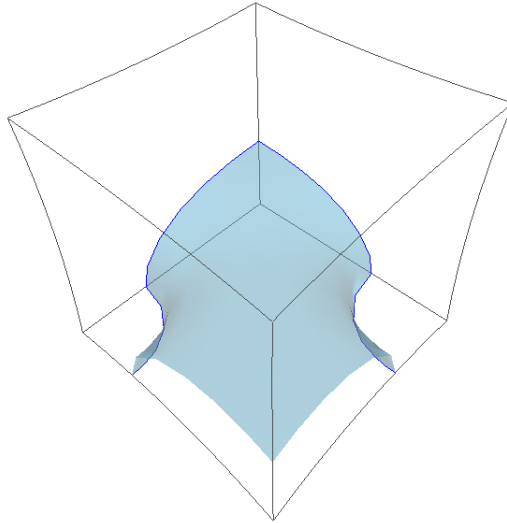


Figure 4.6: The case **aa** plus a discontinuous graph.

A little reflection explains the bad performance of the cases in Fig. 2.4: they make Ω have less contact around O with the fundamental planes compared with any option in Table 2.1. Indeed, the example in Fig. 4.6 is above all others in that table if we look at $V = 0.04$ in Figs. 4.3(b) and 4.4(b). That is why we have not included the cases of Fig. 2.4 in Table 2.1.

Let us now resume our discussion at the beginning of this section. Lawson's result can be found in [20] but for convenience of the reader we shall reproduce it here:

Theorem 4.2. *There exist two doubly periodic surfaces of constant mean*

curvature one and genus two contained in a slab of \mathbb{R}^3 . The ambient translational fundamental cell is a hexagonal or square prism (of infinite height), respectively.

Namely, we had been focusing our attention to just one of Lawson's examples because our study is devoted to the cubic lattice. It is important to mention, however, that in [30, p358] the author comments on some computer simulations for the isoperimetric problem in a skewed Euclidean box. These were performed with the *Surface Evolver* by Pascal Romon (Université Paris-Est Marne-la-Vallée), who has found an isoperimetric surface of genus two [30, Fig.3], precisely the hexagonal example of Theorem 4.2. See [30] for details.

5 Conclusions

As already mentioned, the open question from [29, p.11] has a great chance to be answered in \mathcal{B} according to the evidence shown in Fig. 4.1(c). There the **bdd**-curve is at least 10% above the isop-curve, whereas in the Euclidean case it is only 1.7% above. Indeed, close objects in the Euclidean viewpoint turn out to be farther apart in the hyperbolic geometry. Curiously in both cases the closest approach happens at the turning point between the two surfaces of genus one.

Neither the hyperbolic nor the Euclidean geometry have positive sectional curvatures. The Lawson surfaces have a chance to be isoperimetric in some lens spaces, even though they are just the quotient of \mathbb{S}^3 by a finite cyclic group, which however gives bidirectional translations. Indeed, Γ in Sect. 2 could have been defined just as $\langle T_1, T_2 \rangle$ instead of $\langle T_1, T_2, T_3 \rangle$. In this case **aaa** in Fig. 3.1(a) will rise indefinitely in the vertical direction. The same holds for the examples discussed in [27], [29] but since these works inspired ours we have considered a cubic tessellation.

Regarding $L(p, q)$ we mention the recent result [32], which excludes the Lawson surfaces for infinitely many cases. There the author solves the isoperimetric problem for lens spaces with a large fundamental group:

either geodesic spheres or tori of revolution about geodesics. He also proves that the only candidates in $L(3, q)$ are geodesic spheres of flat tori, $q = 1, 2$.

Notice that such a tessellation exists in \mathbb{S}^3 as it does for \mathbb{H}^3 but without a group that acts totally discontinuously. Hence we cannot have translations because of fixed points. In order to see this, first consider the tiling in Fig. 2.2(b) and the corresponding tiling of \mathbb{S}^2 depicted in Fig. 5.1(a). Of course, compactness implies there are six spherical squares and the south pole is centred at the bottom square, the darkest one in Fig. 5.1(a). Any edge of the tiling belongs to a plane of \mathbb{R}^3 given by $x_i = \pm x_j$, $i \neq j$. Hence continuous displacements that keep the tiling must come from 90° -rotations about the fundamental axes, and any such rotation will have two fixed points.

For the corresponding cubic tessellation of $\mathbb{S}^3 \subset \mathbb{R}^4$ consider $(0, 0, 0, \pm 1)$ as the north \mathcal{N} and south \mathcal{S} poles, respectively. The stereographic projection $\mathbb{S}^3 \setminus \{\mathcal{N}\} \rightarrow \mathbb{R}^3$ that keeps the equator $\mathbb{S}^2 \times \{0\}$ will take its inside to the unit ball in \mathbb{R}^3 , so that \mathcal{S} corresponds to the origin. This ball is shown by grid lines in Fig. 5.1(b), and without loss of generality our tessellation contains the spherical cube centred at \mathcal{S} and depicted there. It has dihedral angle $2\pi/3$, hence by spherical reflections we get eight cubes that cover the whole \mathbb{S}^3 . Now take any spherical displacement that keeps the tessellation. The origin will slide along a fundamental axis but the spherical cubes that are crossed by the other axes will remain invariant. Hence we shall get fixed points in the three-dimensional case as well.

As a matter of fact the unit ball can be viewed as a spherical cube of dihedral angle π , so that together with its reflection in \mathbb{S}^2 one gets a tessellation of \mathbb{S}^3 with only two cubes. However, for a new space form we must take the quotient by the group $\langle id, \mathfrak{A} \rangle$ (identity and antipodal maps). Hence the quotient will have a non-orientable boundary, which is the projective plane. However, the interest in the isoperimetric problem relies mostly on spaces whose geometry fits in the following sequence of generalisations: from Euclidean to spaces forms, from these to homogeneous spaces, and from these to Lie groups in general.

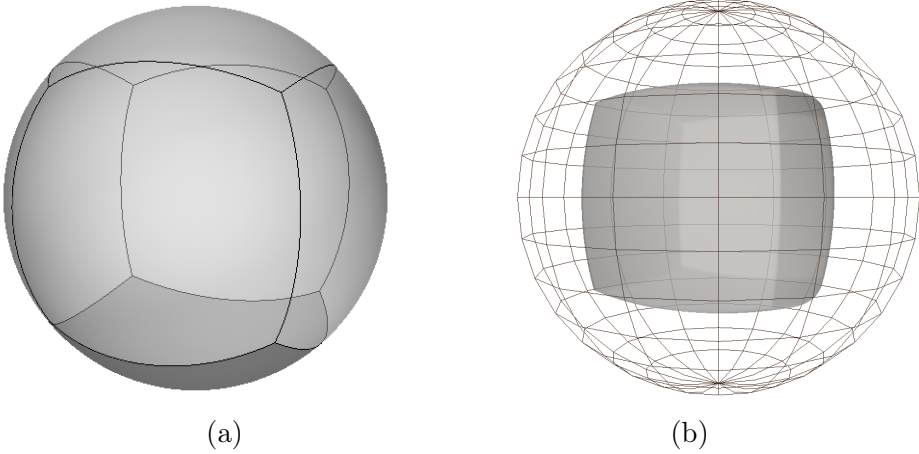


Figure 5.1: The unit ball containing the spherical cube with dihedral angle $2\pi/3$.

This has to do with the amount of results available for these geometries. For instance, in homogeneous spaces we still count on the maximum principle for CMC surfaces, and on the fact that they are minima of area under volume constraint. The *Surface Evolver* works in any finite dimension and it displays three-dimensional projections specified by the user. But of course our understanding and our control of the numerical computation will always work better in the third dimension. There the richest homogeneous spaces have four-dimensional isometry group, and for them much about CMC surfaces is already known. See [23] for a good start.

Acknowledgements

We thank Prof K.Große-Brauckmann at the Maths Dept of the University of Darmstadt for his valuable help in this work. This was during his stay in Brazil in 2010, supported by São Paulo Research Foundation (FAPESP) proc. No. 09/15408-0. We also thank the referees that contributed to the improvement of this paper.

References

- [1] A. D. ALEKSANDROV, Uniqueness theorems for surfaces in the large, *I. Amer. Math. Soc. Transl.* **21**(1962), No. 2, 341–354.
- [2] F. J. ALMGREN, *Existence and regularity almost everywhere of solutions to elliptic variational problems with constraints*, Amer. Math. Soc., Vol. 165, 1976.
- [3] F. BAGINSKI AND K. A. BRAKKE, Deployment analysis of pneumatic envelopes including ascending balloons and inflatable aerodynamic decelerators, *Journal of Spacecraft and Rockets*, **49**(2012), No. 2, 413–421.
- [4] J. L. BARBOSA AND M. DO CARMO, Stability of hypersurfaces with constant mean curvature, *Math. Z.* **185**(1984), 339–353.
- [5] P. BÉRARD, L.L. DE LIMA AND W. ROSSMAN, Index growth of hypersurfaces with constant mean curvature, *Math. Z.* **239** (2002), No. 1, 99–115.
- [6] K. BRAKKE, The Surface Evolver, *Susquehanna University*, (2013).
- [7] K. A. BRAKKE, The Surface Evolver, *Exp. Math.* **1**(1992), No. 2, 141–165.
- [8] ———, Surface Evolver manual, *Mathematics Department, Susquehanna University, Selinsgrove, PA*, **17870**(1994), No. 2.24, 20.
- [9] C. CHEN, P. DURU, M. PRAT, P. JOSEPH, AND S. GEOFFROY, Towards the computation of viscous flow resistance of a liquid bridge, *International Journal of Computational Methods and Experimental Measurements*, **4**(2016), No. 1, 42–49.
- [10] J. CORVINO, A. GEREK, M. GREENBERG, AND B. KRUMMEL, On isoperimetric surfaces in general relativity, *Pacific J. Math.* **231**(2007), No. 1, 63–84.

- [11] S. CUNSOLO, D. BAILLIS, N. BIANCO, V. NASO, M. OLIVIERO, R. LEWIS, AND N. MASSAROTTI, Effects of ligaments shape on radiative heat transfer in metal foams, *International Journal of Numerical Methods for Heat & Fluid Flow*, **26**(2016), No. 2.
- [12] M. P. DO CARMO, AND H. B. LAWSON JR, On Alexandrov-Bernstein theorems in hyperbolic space, *Duke Math. J.*, **50**(1983), No. 4, 995–1003.
- [13] A. E. FABRIS, M. Z. DO NASCIMENTO, AND V. R. BATISTA, A software tool based on the Surface Evolver for precise location of tumours as a preoperative procedure to partial mastectomy, in: *Journal of Physics: Conference Series*, Vol. 633, IOP Publishing, 2015, pp. 012132.
- [14] G. W. GIBBONS, The time symmetric initial value problem for black holes, *Comm. Math. Phys.* **27**(1972), No. 2, 87–102.
- [15] D. GILBARG AND N. S. TRUDINGER, *Elliptic partial differential equations of second order*, Springer, 2015.
- [16] E. GONZALEZ, U. MASSARI, AND I. TAMANINI, On the regularity of boundaries of sets minimizing perimeter with a volume constraint, *Indiana Univ. Math. J.* **32**(1983), No. 1, 25–37.
- [17] K. GROSSE-BRAUCKMANN, Gyroids of constant mean curvature, *Exp. Math.* **6**(1997), No. 1, 33–50.
- [18] M. GRÜTER, Boundary regularity for solutions of a partitioning problem, *Arch. Ration. Mech. Anal.* **97**(1987), No. 3, 261–270.
- [19] W. HSIANG, On generalization of theorems of A. D. Alexandrov and C. Delaunay on hypersurfaces of constant mean curvature, *Duke Math. J.* **49**(1982), No. 3, 485–496.
- [20] H. B. LAWSON JR, Complete minimal surfaces in S^3 , *Ann. of Math.* (1970), 335–374.

- [21] F. MORGAN, Regularity of isoperimetric hypersurfaces in riemannian manifolds, *Trans. Amer. Math. Soc.* **355**(2003), No. 12, 5041–5052.
- [22] R. PENROSE, Naked singularities, *Annals of the New York Academy of Sciences*, **224**(1973), No. 1, 125–134.
- [23] J. PLEHNERT, *Constant mean curvature surfaces in homogeneous manifolds*, Logos Verlag Berlin GmbH, 2012.
- [24] V. RAMOS BATISTA, Theoretical evaluation of elliptic integrals based on computer graphics, *tech. rep.*, 2002 .
- [25] ———, Accurate evaluation of elliptic integrals, *tech. rep.*, 2003 .
- [26] E. RICARDO SA AND E. TOUBIANA, Variants on Alexandrov reflection principle and other applications of maximum principle, *Séminaire de Théorie Spectrale et Géométrie* **19**(2000), 93–121.
- [27] M. RITORÉ CORTÉS, *Superficies con curvatura media constante*, PhD thesis, Universidad de Granada (ES), 1994.
- [28] C. H. RONDON AND V. RAMOS BATISTA, Computational modelling of a spanning drop in a wedge with variable angle, *International Journal of Undergraduate Research and Creative Activities*, **6**(2016), No. 3.
- [29] A. ROS, The isoperimetric problem, in: *Global theory of minimal surfaces*, *Clay Math. Proc.*, Vol. 2, Amer. Math. Soc., Providence, RI, 2001, pp. 175–209.
- [30] ———, Stable periodic constant mean curvature surfaces and mesoscopic phase separation, *Interfaces Free Bound.* **9**(2007), No. 3, 355–365.
- [31] E. SCHMIDT, Beweis der isoperimetrischen Eigenschaft der Kugel im hyperbolischen und sphärischen Raum jeder Dimensionenzahl, *Math. Z.* **49**(1943), No. 1, 1–109.

- [32] C. VIANA, The isoperimetric problem for lens spaces, *Math. Ann.* **374**(2019), No. 1–2, 475–497.